



THE UNIVERSITY *of* EDINBURGH

Edinburgh Research Explorer

Sparsity Driven GMTI Processing Framework with Multichannel SAR

Citation for published version:

Wu, D, Yaghoobi Vaighan, M & Davies, M 2018, 'Sparsity Driven GMTI Processing Framework with Multichannel SAR', *IEEE Transactions on Geoscience and Remote Sensing*.
<https://doi.org/10.1109/TGRS.2018.2866760>

Digital Object Identifier (DOI):

[10.1109/TGRS.2018.2866760](https://doi.org/10.1109/TGRS.2018.2866760)

Link:

[Link to publication record in Edinburgh Research Explorer](#)

Document Version:

Peer reviewed version

Published In:

IEEE Transactions on Geoscience and Remote Sensing

General rights

Copyright for the publications made accessible via the Edinburgh Research Explorer is retained by the author(s) and / or other copyright owners and it is a condition of accessing these publications that users recognise and abide by the legal requirements associated with these rights.

Take down policy

The University of Edinburgh has made every reasonable effort to ensure that Edinburgh Research Explorer content complies with UK legislation. If you believe that the public display of this file breaches copyright please contact openaccess@ed.ac.uk providing details, and we will remove access to the work immediately and investigate your claim.



Sparsity Driven GMTI Processing Framework with Multi-Channel SAR

Di Wu, Mehrdad Yaghoobi, *Member, IEEE*, and Mike Davies, *Fellow, IEEE*

Abstract—This paper presents a processing framework to separate moving targets from the clutter, under multi-channel synthetic aperture radar (SAR) scenarios, and addresses the moving target imaging and velocity estimation problems for ground moving target indication (GMTI) applications. A practical implementation is introduced to break the SAR/GMTI problem into two processing stages, and the sparsity of the moving targets in the observed scene, is exploited throughout the stages. The two stage process extracts the moving targets from the monitored region via a sparsity-based iterative decomposition algorithm, and subsequently estimates the complete velocity vectors of moving targets by enforcing sparsity constraints. The model is sufficiently versatile to incorporate digital elevation map (DEM) information which further improves the moving target relocation accuracy. The effectiveness of the presented framework is demonstrated using Air Force Research Laboratory (AFRL) Gotcha GMTI challenge data.

Index Terms—Synthetic aperture radar (SAR), Ground moving target indication (GMTI), sparsity, compressed sensing, digital elevation map.

I. INTRODUCTION

SYNTHETIC aperture radar (SAR) was first introduced as the remote surveillance instruments to provide high resolution 2D images of the monitored scene with weather-independent, day-or-night surveillance capability. Ground moving target indication (GMTI) techniques can be combined with SAR to pick up moving targets within the formed images and estimate their motion parameters including physical positions and velocities. Since the basic SAR mechanism assumes a stationary scene, a moving target will be displaced and blurred in the formed images. Furthermore, reflected signals from moving targets are buried in the clutter interference which makes targets detection and velocity estimations challenging.

A multi-channel SAR system gives additional features to GMTI applications compared to single-channel methods. For single-channel approaches, slowly moving targets will result in detection difficulties since their Doppler frequency shifts fall into the endo-clutter (mainlobe clutter) spectra. The multi-channel SAR configuration promotes the detection capabilities, and it has smaller minimum detectable velocity (MDV) compared to the single-channel mode [1]. Widely used multi-channel GMTI techniques include image-based subtractive methods, such as Displaced Phase Center Antenna (DPCA) and Along Track Interferometry (ATI) [2][3], and raw-data-based approaches, such as Space-time Adaptive Processing (STAP) and imaging STAP (ISTAP) [4][5]. In particular, DPCA suppresses the clutter based on magnitude in the image domain, and ATI reveals moving targets via the interference

phases between different radar channels. STAP is an adaptive filtering technique that realises the GMTI tasks by solving a computational expensive statistical test problem. It is worth mentioning that these approaches have been proven to work properly under a homogeneous clutter assumption. However, for non-homogeneous terrains, such as mountains with large terrain variations and urban regions with strong building scatterers, the aforementioned methods may miss the detections and advanced techniques are needed to be employed [6]. Recent developments in SAR/GMTI involve the extensions of DPCA (EDPCA) [7], hybrid techniques that use DPCA and ATI [1], and sparsity based approaches [8][9].

A. Main Contribution

In this paper we introduce a sparsity based framework for multi-channel SAR-based GMTI applications. A fundamental additive model is assumed, (1), such that the SAR image $\mathbf{X} \in \mathbb{C}^{M \times L}$ can be decomposed into the background image (static reflectors) \mathbf{X}_s and the dynamic image \mathbf{X}_d (moving targets).

$$\mathbf{X} = \mathbf{X}_s + \mathbf{X}_d \quad (1)$$

By leveraging the sparsity of \mathbf{X}_d , i.e. the moving targets are sparse in the monitored scene, the GMTI task can be formulated as a sparsity regularised optimisation problem to separate \mathbf{X}_d from \mathbf{X}_s , and estimate the moving target states, i.e. their locations, reflectivities and velocities. Unlike conventional clutter suppression methods such as DPCA and ATI which are mainly based on detecting the moving targets, the presented framework is capable of decoupling the moving target signal and the strong background clutter, and it provides further potential to implement subsequent automatic target recognition (ATR), or even inverse SAR on the extracted moving targets. In addition, we show that the framework is sufficiently versatile to incorporate the DEM which further improves the moving target relocation accuracy especially when significant elevation variations exist.

Consider the typical SAR-based GMTI tasks of image formation, target indication, and state estimation. The proposed sparsity based framework is designed to integrate these GMTI goals into an optimisation problem regularised by target sparsities, and it serves as a generic model for tackling these problems which can also incorporate other SAR imaging algorithms. However, solving the optimisation problem within one processing stage is very challenging as the target locations change as a function of their estimated velocities. Therefore in this paper, a practical solution is to break the problem into a two stage process where we first utilise target sparsities

to separate the blurred and displaced moving targets from the static background scene and subsequently relocate and refocus individual moving targets, again exploiting the sparsity constraint. While the two stage process sacrifices a degree of sparsity (the blurred targets are less sparse than the correctly focused ones), it results in a simpler more tractable problem. Compared to the preliminary work on this topic [8][10], this paper presents a complete SAR/GMTI processing pipeline and a more robust implementation for tackling the model. We also consider the DEM information throughout the pipeline and provide solid experimental results via the real AFRL GOTCHA GMTI challenge data [11].

Overall, the contributions of this work are:

1. a novel sparsity-aided framework which integrates the SAR/GMTI missions, i.e. SAR imaging, moving target and background decomposition, and target state estimation, into optimisation problems,
2. practical implementation of the proposed framework with a two stage process and theoretically/experimentally proven algorithms,
3. incorporation of a DEM model into the SAR-based GMTI processing. Although the focus here is on enhancing the proposed sparsity-based SAR/GMTI framework, the exploitation of the DEM in other SAR/GMTI algorithms may be of independent interest.

B. Structure of This Paper

The remainder of paper is organized as follows. Section II describes the signal modeling of a typical multi-channel SAR system with a specific terrain map. The geometry of the spotlight airborne SAR system is depicted and the received SAR data model is introduced. In section III we mainly focus on the proposed sparsity-driven SAR-based GMTI processing. We start by discussing the pre-processing methods of SAR raw data. Then the SAR imaging and GMTI basics are introduced. We also present the motivation of using sparsity in SAR-based GMTI and how it differs from existing methods. By considering the priori information (e.g. sparsity) involved in the moving target characteristics, we introduce detailed implementations of the proposed SAR/GMTI framework. A robust moving targets and background decomposition algorithm is presented, and the mechanism of the ground moving target imaging and motion parameter estimation using sparsities is explained in detail.

We demonstrate the performance of the proposed approach through real multi-channel airborne SAR data in section IV. Here the AFRL Gotcha GMTI challenge data which contains a known moving vehicle in the urban environment is investigated and the complete processing pipeline is presented. We show the formed DEM aided images of both the moving targets and background. We also compare the proposed method with other GMTI approaches in this section, and report the differences on the estimated target locations and velocities. Future work and conclusions are summarized in section V.

GLOSSARY

\mathbf{X} the complex SAR image.

\mathbf{X}_d the SAR image of the moving targets.

\mathbf{X}_s the SAR image of the background.

\mathbf{Y}_i the 2-D phase history for the i -th channel.

$\tilde{\mathbf{Y}}_i$ the pre-processed phase histories of the i -th channel.

$\mathbf{V}^{(x)}$ the x-direction velocities of the image pixels ($\mathbf{V}^{(y)}$ and $\mathbf{V}^{(z)}$ likewise).

\mathbf{V} the velocity map ($\mathbf{V}^{(x)}, \mathbf{V}^{(y)}, \mathbf{V}^{(z)}$) of the whole observed scene.

\mathbf{P} the phase correction matrix on \mathbf{X}_d between different channels.

\mathbb{G}_{ml} the discrete grid on which the SAR image is formed.

g_i the antenna gain of the i -th channel.

σ the reflectivity of the moving target.

c the velocity of light.

f_k the discrete range frequencies.

τ_n the discrete slow time with pulse number n .

d the channel spacing.

f_{PRF} the system pulse repetition frequency (PRF).

\mathbf{r} the instantaneous position vector of the platform.

$\mathbf{r}_i^{(t)}$ the vector from the i -th antenna to the moving target.

$\mathbf{r}_i^{(o)}$ the vector from the i -th antenna to the origin.

\mathbf{v}_t the vector that represents the moving target velocity.

$\mathbf{v}^{(r)}$ the vector that represents the radial velocity of the target.

\mathbf{v}_p the vector that represents the platform velocity.

\mathbf{H} the channel balancing matrix in the Doppler and range frequency domain.

$Q_i(\Omega)$ the channel-dependent term in \mathbf{Y}_i with the range frequency Ω .

$D_i(\omega)$ the antenna pattern in \mathbf{Y}_i with the Doppler frequency ω .

$\|\cdot\|_F$ the Frobenius norm.

\mathcal{N} the element-wise normalisation operator.

\odot the element-wise product operator.

\oslash the element-wise division operator.

$\langle \cdot, \cdot \rangle$ the dot product operator.

II. GEOMETRY AND SIGNAL MODELING

A typical multi-channel SAR system which operates in the spotlight mode is depicted in Fig. 1, where the observed scene contains a number of moving targets. A terrain map that contains elevation information on the z direction is associated with the illuminated region. An airborne platform carries multiple radar channels which are equally positioned with a distance d along the flight path. In the rest of the paper, bold letters denote vectors and matrices and non-bold ones denote scalars. Specifically, the non-bold term is the Euclidean norm of the bold one with the same name. Let $\mathbf{v}_t = (v^{(x)}, v^{(y)}, v^{(z)})$ be the velocity vector of a moving target in the scene, whereas $\mathbf{v}^{(r)}$ and $\mathbf{v}^{(az)}$ denote its corresponding radial and azimuth velocity respectively. τ_n represents the slow (azimuth) time of the transmitted pulses where $n = \{1, 2, \dots, N\}$ is the pulse number. We denote $r_i^{(t)}(\tau_n)$ (the norm of $\mathbf{r}_i^{(t)}(\tau_n)$) as the distance between this target and the i -th antenna. Similarly $r_i^{(o)}(\tau_n)$ is the distance from the scene center to the i -th channel. The platform velocity v_p is assumed to be a constant within a short enough sub-aperture.

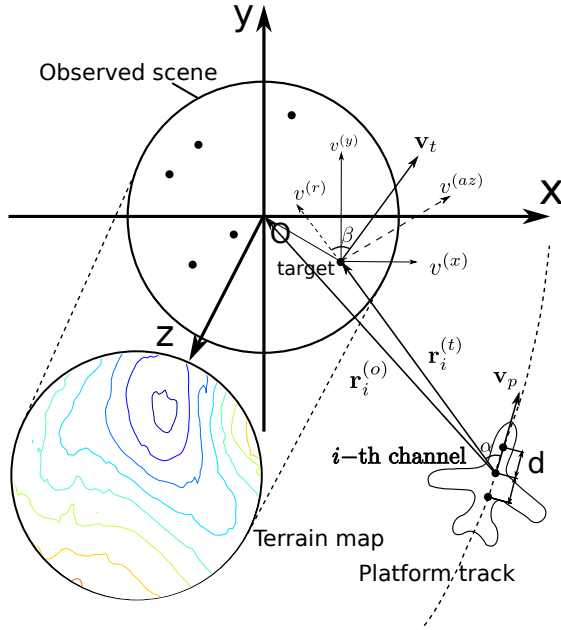


Fig. 1: The geometry of a typical multi-channel SAR system in the spotlight mode. A number of moving targets are present and the observed scene is associated with a digital elevation map.

We consider the moving target with the reflectivity σ in Fig. 1 to illustrate the signal model. After the de-chirping process (the scene origin is calibrated to have zero phase) and discretization, by defining K as the number of range frequency samples in the phase history and N as the number of azimuth samples, the received signal for the i -th antenna from this target is a $K \times N$ complex matrix which can be modeled as:

$$\mathbf{Y}_i(f_k, \tau_n) = g_i \sigma \exp\left(-\frac{j4\pi f_k u_i(\tau_n)}{c}\right) \quad (2)$$

where $\{f_k | k = 1, 2, \dots, K\}$ denotes the range frequencies and $u_i(\tau_n)$ represents the differential range $r_i^{(t)}(\tau_n) - r_i^{(o)}(\tau_n)$. Given that $\mathbf{X} \in \mathbb{C}^{M \times L}$ (the imaging scene is defined on the M -by- L discrete grid) is the collection of the reflectivities from all targets (both static and moving) in the scene with the constant antenna gain, the received phase history can be assembled by accumulating the reflected signals from all reflectors:

$$\mathbf{Y}_i(f_k, \tau_n) = \sum_{m=1}^M \sum_{l=1}^L \mathbf{X}(m, l) \exp\left(-\frac{j4\pi f_k u_{mli}(\tau_n)}{c}\right) \quad (3)$$

Here $u_{mli}(\tau_n)$ represents the differential range with respect to the reflector at (m, l) . The signal model (3) can be rewritten in the matrix-vector form as $\mathbf{Y}_i = \Phi_F(\mathbf{X})$, where $\mathbf{Y}_i \in \mathbb{C}^{K \times N}$ is the 2-D phase history for the i -th channel and Φ_F denotes the forward operator that projects the reflectivities to the phase history. More generally, for small sub-apertures the distance measure $u_{mli}(\tau_n)$ can incorporate velocities. To avoid ambiguities, we denote $\Phi_F^{\mathbf{V}}$ and Φ_F^0 as the forward operators for all targets with the velocity map described by $\mathbf{V} = (\mathbf{V}^{(x)}, \mathbf{V}^{(y)}, \mathbf{V}^{(z)})$ and the static scene respectively. The

$\Phi_B^{\mathbf{V}}$ and Φ_B^0 are the inverse operators of $\Phi_F^{\mathbf{V}}$ and Φ_F^0 which project from the received signals to reflectivities (details can be found in section III).

In fact $r_i^{(t)}(\tau_n)$ indicates how the distance from the antenna to the target varies with time, and it depends on three components, i.e. the platform velocity \mathbf{v}_p , the target velocity \mathbf{v}_t and the channel positions.

Let

$$\begin{aligned} r_i^{(t_1)}(\tau_n) &= -v_p \cos(\alpha) \tau_n \\ r_i^{(t_2)}(\tau_n) &= v_t \cos(\beta) \tau_n \\ r_i^{(t_3)}(\tau_n) &= \cos(\alpha)(i-1)d \end{aligned} \quad (4)$$

where α defines the angle between the radar-target vector and the platform velocity vector ($\cos(\alpha) = \langle \mathbf{v}_p / v_p, \mathbf{r}_i^{(t)} / r_i^{(t)} \rangle$), β denotes the angle between the radar-target vector and the target velocity vector ($\cos(\beta) = \langle \mathbf{v}_t / v_t, \mathbf{r}_i^{(t)} / r_i^{(t)} \rangle$), and $r_i^{(t_1)}(\tau_n)$, $r_i^{(t_2)}(\tau_n)$ and $r_i^{(t_3)}(\tau_n)$ account for the variations on $r_i^{(t)}(\tau_n)$ induced by the platform velocity, target velocity and channel number respectively.

Within a short sub-aperture, the varying range between the target and platform $r_i^{(t)}(\tau_n)$ can be approximated with

$$r_i^{(t)}(\tau_n) \approx r_1^{(t)}(0) + r_1^{(t_1)}(\tau_n) + r_1^{(t_2)}(\tau_n) + r_i^{(t_3)}(\tau_n) \quad (5)$$

where the constant $r_1^{(t)}(0)$ corresponds to the distance from the first channel at the initial position of the sub-aperture to the target. Similarly we can decompose $r_i^{(o)}(\tau_n)$ into three components with an additional constant, and thus implement an expansion on (2) given that $u_i(\tau_n) = r_i^{(t)}(\tau_n) - r_i^{(o)}(\tau_n)$. It can be seen from (5) that $r_i^{(t_3)}(\tau_n)$ is the dominating channel number related term. These formulations offer us further insight into how different radar channels and the target-platform relative movement function in the signal model, and can be exploited to pre-process SAR data.

III. SPARSITY BASED GMTI

This section investigates the sparse modalities in SAR-based GMTI applications. We develop a novel SAR/GMTI framework and show that the target sparsities can be exploited to help decouple moving targets and background, and estimate moving target states. In addition, the essential pursuit of GMTI methods and the use of DEM are discussed. The entire flowchart of the processing pipeline is illustrated in Fig. 2. It is worth mentioning that the two processing stages are both exploiting the target sparsities and they can be formulated as one optimisation problem. Here we break the framework into a two stage process as a more tractable solution.

A. Data Pre-processing

We first discuss the pre-processing of the received phase histories based on the aforementioned side-looking multi-channel SAR scenario. The task is to implement a channel calibration to acquire the same responses for static reflectors among different channels. An adaptive 2-D channel balancing technique was introduced in [12][13] to tackle this problem. We apply this method to the SAR pre-processing in the remainder of

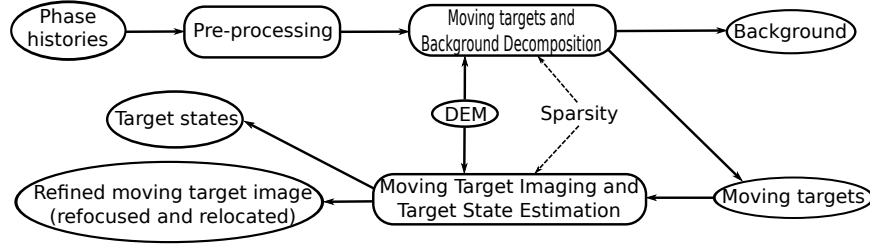


Fig. 2: The flowchart of the sparsity driven SAR/GMTI processing framework. It provides multiple features including the separation of moving targets and background, the moving target imaging, and the target velocity estimation. The DEM information is also exploited.

the paper. Consider (2), (4) and (5), the relative movement between the platform and target will introduce a channel related calibration term $\exp(-j4\pi r_i^{(t_3)}(\omega)/\lambda) = \exp(-j(i-1)\omega d/v_p)$ (by inserting (4)) to the Doppler transformed signal where λ is the corresponding wavelength and ω is the Doppler frequency. If we put aside the moving targets, we have two channel related facets which influence the Doppler frequency domain signal, i.e. the antenna characteristics g_i and the channel spacing d . In general, the Fourier transformed signals in the continuous Doppler and range frequency domain (ω, Ω) have the following form [13]:

$$\mathbf{Y}_i(\omega, \Omega) \cong A(\omega)Q_i(\Omega)D_i(\omega)\exp(-j\frac{(i-1)d}{v_p}\omega) \quad (6)$$

where $A(\omega)$ is the nominal factor that denotes the complex Doppler dependencies. This approximation holds when the observed scene is dominated by the stationary background.

It can be seen from (6) that the Doppler related terms are approximately independent of the range frequency related terms (it holds for the SAR mode with small squint angles). Therefore, the phase histories can be calibrated with two functions in azimuth and range directions, e.g. the $H_{az}(\omega)$ and $H_{rg}(\Omega)$ in (7), to acquire the same responses from static reflectors for a pair of channels. The calibration functions for the i -th and k -th channels are:

$$\begin{aligned} H_{az}(\omega) &= \frac{D_i(\omega)}{D_k(\omega)} e^{j(k-i)\omega d/v_p} \\ H_{rg}(\Omega) &= \frac{Q_i(\Omega)}{Q_k(\Omega)} \end{aligned} \quad (7)$$

We denote $\hat{\mathbf{Y}}_i$ as the Fourier transformed \mathbf{Y}_i in the Doppler and range frequency domain. The phase history for the k -th channel can then be balanced via $\hat{\mathbf{Y}}_k \odot \mathbf{H}$ where $\mathbf{H}(\omega, \Omega) = H_{az}(\omega)H_{rg}(\Omega)$. We therefore have the channel balancing matrix \mathbf{H} as a rank one matrix. The balanced phase histories can be transformed back to the (f_k, τ_n) domain and we denote the pre-processed phase histories of the k -th channel as $\tilde{\mathbf{Y}}_k$. Therefore, the channel balancing can be performed pair-wise. The channel balancing step plays a vital role in subtractive GMTI algorithms such as DPCA and ATI which pick up moving targets through the coherent differences between channels. Inaccurate calibrations will lead to imperfect subtractions and

increase the false alarm rates. In practice \mathbf{H} can be estimated via:

$$\min_{\mathbf{H}} \frac{1}{2} \|\hat{\mathbf{Y}}_i - \hat{\mathbf{Y}}_k \odot \mathbf{H}\|_F^2 \quad (8)$$

for which a viable solution is presented in [13].

Note that more azimuth samples lead to refined accuracy in estimating $H_{rg}(\Omega)$. However, high fidelity will be preserved only for the azimuth samples in low frequencies as $H_{az}(\omega)$ has significant attenuation in amplitudes with azimuth frequencies. In this paper we estimate $H_{az}(\omega)$ and $H_{rg}(\Omega)$ over sub-apertures (8000 pulses), and abandon the high frequency parts (7200 azimuth frequencies) in $H_{az}(\omega)$.

B. SAR Imaging and GMTI

The SAR image formation algorithms are essentially solving the following optimisation problem:

$$\min_{\mathbf{X}} \frac{1}{2} \|\mathbf{Y}_i - \Phi_F(\mathbf{X})\|_F^2. \quad (9)$$

Conventional SAR imaging approaches originated from the attempt to approximate the pseudo inverse of the forward projection operator Φ_F^0 . Take the well known matched filter and back projection algorithms as some examples. They realise the image formation via $\mathbf{X} = \Phi_B^0(\mathbf{Y}_i)$, where the backward projection operator Φ_B^0 is the Hermitian transpose of Φ_F^0 in the sense of matrices:

$$\mathbf{X}(m, l) = \sum_{k=1}^K \sum_{n=1}^N Y_i(f_k, \tau_n) \exp\left(\frac{j4\pi f_k \Delta \mathbf{R}_{mln}}{c}\right) \quad (10)$$

associated with the discrete grid, $\mathbb{G}_{ml} = (x_m, y_l, z_{ml})$, on which the SAR image is formed, where $m = \{1, 2, \dots, M\}$, $l = \{1, 2, \dots, L\}$, z_{ml} is the DEM associated with (x_m, y_l) . The differential ranges $\Delta \mathbf{R}_{mln}$ are:

$$\Delta \mathbf{R}_{mln} = \|\mathbf{r}(\tau_n) - \mathbb{G}_{ml}\|_2 - \mathbf{R}_0(\tau_n) \quad (11)$$

where $\mathbf{R}_0(\tau_n) = \|\mathbf{r}(\tau_n) - \mathbf{r}_{ref}\|$ denotes the distance as a function of azimuth time between the platform and a reference point \mathbf{r}_{ref} (usually the scene center). For the rest of the paper, we employ a fast back projection approach [14] for the SAR imaging operator Φ_B^0 which is an accurate and efficient approximation of (10).

In SAR imaging, multiple target detection algorithms have been proposed to identify the ground moving targets within the formed images. In particular, DPCA is implemented through

the subtraction of the formed SAR images between different channels, ATI is realised by multiplying the formed image from one channel with the conjugate of the complex image from another channel, and a recent compressed sensing based method exploited the pixel-wise sparsity of the moving targets in the image domain [9].

In general, these GMTI techniques can be taken as the post-processing of the SAR images. They are capable of detecting displaced targets in SAR images and estimating their radial velocities. Since the SAR image formation is essentially based on minimising an objective function (9), we are motivated to incorporate the GMTI features into the SAR imaging optimisation framework and thus implement the GMTI tasks simultaneously within the imaging step. Compared to the conventional SAR-base GMTI processing chain, we aim to develop an end-to-end framework from the optimisation perspective. Furthermore, conventional DPCA and ATI algorithms mainly focus on target detection using subtractive approaches between channels and are not designed to realise an exact moving target and background decomposition. We next introduce the proposed SAR/GMTI framework in detail.

C. Moving Targets and Background Decomposition

The flowchart of the moving targets and background decomposition stage can be visualised via Fig. 3. We first introduce a variable splitting approach (1) to the SAR image domain, and denote $\mathbf{X}_s \in \mathbb{C}^{M \times L}$ and $\mathbf{X}_d \in \mathbb{C}^{M \times L}$ as the static background and moving (displaced and blurred targets) target reflectivities for the first channel, respectively. Motivated by the fact that the formed images of one moving target with neighbouring channels have a phase difference $(4\pi/c)f_0 v^{(r)}(d/v_p)$ (f_0 is the central frequency of the transmitted signal) which encodes the target radial velocity, we can then introduce a phase correction matrix \mathbf{P} that enables us to describe the dynamic image in the other channels. Specifically \mathbf{X}_d can be assumed to be sparse given that there are typically few spatially localized moving targets in the observed scene (\mathbf{X}_d is assumed to have at most s non-zero entries).

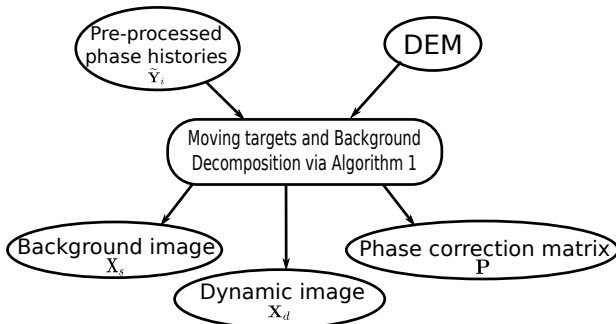


Fig. 3: The moving targets and background decomposition stage of the proposed framework.

The moving targets and background decoupling model can

be described as:

$$\begin{aligned}
 \min_{\mathbf{X}_s, \mathbf{X}_d, \mathbf{P}} \quad & \frac{1}{2} \sum_i \|\tilde{\mathbf{Y}}_i - \Phi_F^0(\mathbf{X}_s + \mathbf{X}_d \odot \mathbf{P}^{i-1})\|_F^2 \\
 \text{s.t.} \quad & \|\mathbf{X}_d\|_0 \leq s \\
 & \text{supp}(\mathbf{X}_d) = \text{supp}(\mathbf{P} \cdot \mathbf{1}) \\
 & |\mathbf{P}_{ml}| = 1, m = 1, \dots, M, l = 1, \dots, L
 \end{aligned} \tag{12}$$

where $\mathbf{P} \in \mathbb{C}^{M \times L}$ is the phase correction matrix on \mathbf{X}_d which has element-wise magnitude 1 entries (e.g. the stationary reflectors off the support of \mathbf{X}_d have zero phase shifts $\mathbf{P}_{ml} = \exp(j0) = 1$), the moving target reflectivities in \mathbf{X}_d are assumed to be s -sparse, and $\text{supp}(\mathbf{X}_d)$ stands for the support set of \mathbf{X}_d indicating the non-zeros in \mathbf{X}_d . As shown above, the radial velocity of the target is encoded in the phase of \mathbf{P} . \mathbf{X}_d and $\mathbf{P} \cdot \mathbf{1}$ have the same support on the pixels which form the moving targets, and $\mathbf{P} \cdot \mathbf{1}$ is thus s -sparse as well. We assume that the channel phase centers are equally spaced and define \mathbf{P}^i as:

$$\mathbf{P}^i = \underbrace{\mathbf{P} \odot \dots \odot \mathbf{P}}_i \tag{13}$$

where $i > 0$ and $\mathbf{P}^0 = \mathbf{1}$.

By leveraging the sparsity of the moving targets and maintaining the data fitting fidelity, the presented model (12) retrieves the formed images for both moving targets \mathbf{X}_d and background \mathbf{X}_s , and simultaneously estimates a phase correction matrix \mathbf{P} . Practically \mathbf{P} leads to the direct estimation of the radial velocities of the moving targets. Note that \mathbf{X}_d corresponds to the displaced and blurred moving targets without considering for the velocity components. A variant of (12) can be formulated by considering full target velocity vectors, and the state estimation of moving targets is thus simultaneously realised in this processing stage. However, the target locations change as a function of their estimated velocities and there is a lack of computationally effective forward/backward projection operators to handle all moving targets simultaneously. This difficulty drives us to put aside the full target velocity vectors in (12) and employ the moving target state estimation in the subsequent step.

Since (12) is a challenging non-convex optimisation problem, we reformulate it for a more practical implementation. To simplify tackling this non-convex optimisation, we first introduce the intermediate variables $\mathbf{dX}^1 = \mathbf{X}_d \odot \mathbf{P} - \mathbf{X}_d = \mathbf{X}_d \odot (\mathbf{P} - \mathbf{1})$ and $\mathbf{X}_1 = \mathbf{X}_s + \mathbf{X}_d$. These let us to establish good initialisations with DPCA and ATI algorithms. Particularly \mathbf{dX}^1 can be taken as the differences between the SAR images of the 2-nd and 1-st channels, and \mathbf{X}_1 corresponds to the reconstructed SAR image based on the first channel. Therefore \mathbf{dX}^1 and \mathbf{X}_1 can be initialised with the DPCA and back-projection algorithms. Note that we have the bijective mapping from the variable set $\{\mathbf{X}_s, \mathbf{X}_d, \mathbf{P}\}$ to $\{\mathbf{X}_1, \mathbf{dX}^1, \mathbf{P}\}$. We then propose an alternating update mechanism on \mathbf{X}_1 , \mathbf{P} and \mathbf{dX}^1 that alternately updates one of them at a time, while keeping the others fixed. With I

radar channels (12) can be rewritten as:

$$\begin{aligned} & \min_{\mathbf{X}_1, \mathbf{dX}^1, \mathbf{P}} \frac{1}{2} \|\tilde{\mathbf{Y}}_1 - \Phi_F^0(\mathbf{X}_1)\|_F^2 + \\ & \frac{1}{2} \sum_{i=2}^I \|\tilde{\mathbf{Y}}_i - \Phi_F^0(\mathbf{X}_1 + \sum_{j=1}^{i-1} \mathbf{dX}^1 \odot \mathbf{P}^{j-1})\|_F^2 \\ & \text{s.t.} \quad \|\mathbf{P} - \mathbf{1}\|_0 \leq s \\ & \quad \text{supp}(\mathbf{dX}^1) = \text{supp}(\mathbf{P} - \mathbf{1}) \\ & \quad |\mathbf{P}_{ml}| = 1, \quad m = 1, \dots, M, \quad l = 1, \dots, L \end{aligned} \quad (14)$$

Since we have $\|\mathbf{X}_d\|_0 = \|\mathbf{P} - \mathbf{1}\|_0 = \|\mathbf{dX}^1\|_0$ and equal supports, the sparsity constraint can be introduced to assume that $\mathbf{P} - \mathbf{1}$ has no more than s non-zeros.

The detailed implementation of the proposed decomposition method can be found in Algorithm 1. Through the iterations, \mathbf{X}_1 is updated along the negative gradient direction, the phase correction matrix \mathbf{P} is updated with gradient decent methods followed by an element-wise projection onto the unit ball and thresholding operations [15] on $\mathbf{P} - \mathbf{1}$ (the cost function is non-increasing with appropriate step sizes as shown in [16]), and \mathbf{dX}^1 is computed using gradient decent methods while its support is limited by $\text{supp}(\mathbf{dX}^1) = \text{supp}(\mathbf{P} - \mathbf{1})$. Throughout the algorithm, the final support of \mathbf{dX}^1 and $\mathbf{P} - \mathbf{1}$ are achieved by iteratively thresholding $\mathbf{P} - \mathbf{1}$. As the magnitudes of the elements of $\mathbf{P} - \mathbf{1}$ are bounded between 0 and 2, and \mathbf{X}_d has no upper bound for its magnitudes, one advantage of thresholding $\mathbf{P} - \mathbf{1}$ is that it prevents the elements of \mathbf{X}_d from having excessive magnitudes, when we estimate \mathbf{X}_d based on $\mathbf{P} - \mathbf{1}$.

To achieve accurate approximations within a few iterations, we initialise \mathbf{dX}^1 with the DPCA algorithm using the first two channels, \mathbf{X}^1 using the back-projection algorithm on the first channel, and \mathbf{P} with $\mathcal{N}(\Phi_B^0(\tilde{\mathbf{Y}}_3 - \tilde{\mathbf{Y}}_2) \odot \Phi_B^0(\tilde{\mathbf{Y}}_2 - \tilde{\mathbf{Y}}_1))$ respectively, where \mathcal{N} is the normalisation operator ($\mathcal{N}(\mathbf{P}) = \mathbf{P} \odot |\mathbf{P}|$) to preserve the phases and \mathbf{P} indicates the conjugated \mathbf{P} . $|\cdot|^k$ stands for the corresponding variable in the k -th iteration. γ_1 , Γ_2 and γ_3 are the step sizes in the gradient descent directions. A threshold value ψ can be tuned to threshold the estimated \mathbf{X}_d for improved visualisation. If \mathbf{a} is an arbitrary vector, the hard-thresholding operator $\mathcal{T}(\mathbf{a}, \psi)$ can be defined so that all the elements in \mathbf{a} below ψ (in magnitude) are set to zero. Practically the value of ψ is driven by the level of noise in the data to best approximate the SAR image of moving targets \mathbf{X}_d . To eliminate the small values in \mathbf{X}_d without significant signal attenuation, ψ can be 0 or a very small value for subsequent processing. The value of ψ will depend on the specific SAR scenario, and instead of assigning a constant value to ψ , we tune ψ to be proportional to the energy of \mathbf{X}_d , i.e. $\|\mathbf{X}_d\|_F$. In particular, for the real data in this work, $\psi < 0.5\% \|\mathbf{X}_d\|_F$ has achieved acceptable performance in our experiments.

For a three-channel SAR system, in this paper, we approximate the step sizes with $\gamma_1 = \|\tilde{\mathbf{Y}}_1\|_F^2 / \|\Phi_B^0(\tilde{\mathbf{Y}}_1)\|_F^2$, $\Gamma_2 = \|\tilde{\mathbf{Y}}_1\|_F^2 / \|\Phi_B^0(\tilde{\mathbf{Y}}_1)\|_F^2 \odot |\mathbf{dX}^1|^2$ and $\gamma_3 = \|\tilde{\mathbf{Y}}_1\|_F^2 / \|\Phi_B^0(\tilde{\mathbf{Y}}_1)\|_F^2 / 2$ based on the spectral norm argument given in [17]. Note that these step sizes play a crucial role in the performance of gradient descent methods. Although these step sizes work well in practice to decrease

the objective function, to rigorously guarantee the non-increasing of the cost function, we can employ the following backtracking mechanism at the end of each iteration. Let $f(\mathbf{X}_1, \mathbf{dX}^1, \mathbf{P})$ be the objective function in (14). Whenever we find that $f(\mathbf{X}_1|^{k+1}, \mathbf{dX}^1|^{k+1}, \mathbf{P}|^{k+1}) > f(\mathbf{X}_1|^{k+1}, \mathbf{dX}^1|^{k+1}, \mathbf{P}|^k)$ at the end of iteration, we restart the k -th iteration with halved γ_1 , Γ_2 and γ_3 . Similarly we employ the backtracking mechanism for updating \mathbf{P} because of the complicated constraints on it, i.e. in (15) we estimate $\mathbf{P}|^{k+1}$ with the weighted combination of the new estimate and previous estimate $\mathbf{P}|^k$, and $\mathbf{P}|^{k+1}$ is re-estimated with halved λ if $f(\mathbf{X}_1|^{k+1}, \mathbf{dX}^1|^{k+1}, \mathbf{P}|^{k+1}) > f(\mathbf{X}_1|^{k+1}, \mathbf{dX}^1|^{k+1}, \mathbf{P}|^k)$.

The update equations for \mathbf{P} and \mathbf{dX}^1 are defined as follows:

$$\mathbf{P}_{ml}|^{k+1} = \begin{cases} \lambda \times \mathcal{N}(\mathbf{P}_{ml}|^{k+0.5}) + (1 - \lambda) \times \mathbf{P}_{ml}|^k & |\mathcal{N}(\mathbf{P}_{ml}|^{k+0.5}) - \mathbf{1}| > \varphi \\ 1 & \text{otherwise} \end{cases} \quad (15)$$

$$\mathbf{dX}_{ml}^1|^{k+1} = \begin{cases} \mathbf{dX}_{ml}^1|^{k+0.5} & \mathbf{P}_{ml}|^{k+1} \neq 1 \\ 0 & \text{otherwise} \end{cases} \quad (16)$$

where λ (default value is 1) is used for the backtracking mechanism. φ is the constant controlling the sparsity of moving targets (φ is 0.5 in this paper for consistency).

D. Required Number of Channels

It is worth mentioning that at least three channels are required to complete the task of decoupling moving targets and the background. With less channels the feasible set (assuming exact data fidelity) would be the whole space and therefore there would not be enough constraints to identify the sparse moving targets. Consider a simple three-channel SAR system with a single moving target at position (m, l) , we denote \mathbf{X}_i ($i = \{1, 2, 3\}$) as the reconstructed reflectivities for the i -th channel. Therefore we have the equations:

$$\begin{aligned} \mathbf{X}_1(m, l) &= \mathbf{X}_s(m, l) + r \\ \mathbf{X}_2(m, l) &= \mathbf{X}_s(m, l) + rq \\ \mathbf{X}_3(m, l) &= \mathbf{X}_s(m, l) + rq^2 \end{aligned} \quad (17)$$

where $r \in \mathbb{C}$ is the reflectivity of the target, and $q \in \mathbb{C}$ is the phase correction of the target between channels which lies on the unit ball.

Based on the reflectivities \mathbf{X}_i , (17) would be enough to retrieve the three unknowns $\mathbf{X}_s(m, l)$, r and q . However, if we are given only the first two channels (the first two equations in (17)), we can only estimate r and q as long as $r \gg \mathbf{X}_s(m, l)$ (this is essentially ATI assumption) via:

$$\begin{aligned} r &= \mathbf{X}_1(m, l) \\ \mathbf{X}_s(m, l) &= 0 \\ q &= \mathbf{X}_2(m, l) / \mathbf{X}_1(m, l) \end{aligned} \quad (18)$$

However, when $\mathbf{X}_s(m, l)$ is not negligible, (18) is inaccurate and we have ambiguities in estimating $\mathbf{X}_s(m, l)$, r and q . Therefore q and the radial velocity of the target cannot be

Algorithm 1 : Iterative algorithm for approximating the solution of (14).

-
- 1: {Initialisation} $k \leftarrow 1$; $\mathbf{X}_1|^{(k)} \leftarrow \gamma_1 \Phi_B^0(\tilde{\mathbf{Y}}_1)$; $\mathbf{P}|^{(k)} \leftarrow \mathcal{N}(\Phi_B^0(\tilde{\mathbf{Y}}_3 - \tilde{\mathbf{Y}}_2) \odot \Phi_B^0(\tilde{\mathbf{Y}}_2 - \tilde{\mathbf{Y}}_1))$; $\mathbf{dX}^1|^{(k)} \leftarrow \gamma_1 \Phi_B^0(\tilde{\mathbf{Y}}_2 - \tilde{\mathbf{Y}}_1)$; $\mathbf{X}_d \leftarrow \mathbf{0}$
 - 2: **while** $k < K$ **do**
 - 3: {Updating \mathbf{X}_1 } $\mathbf{X}_1|^{(k+1)} \leftarrow \mathbf{X}_1|^{(k)} - \frac{\gamma_1}{3} \times$
 $\Phi_B^0\left(\Phi_F^0\left(I \times \mathbf{X}_1|^{(k)} + \sum_{i=1}^{I-1} (i \times \mathbf{dX}^1|^{(k)} \odot \mathbf{P}^{I-1-i}|^{(k)}) - \sum_{i=1}^I \tilde{\mathbf{Y}}_i\right)\right)$
 - 4: {Updating \mathbf{P} } $\mathbf{P}|^{(k+0.5)} \leftarrow \mathbf{P}|^{(k)} - \Gamma_2 \odot$
 $\sum_{i=3}^I \left(\Phi_B^0\left(\Phi_F^0\left(\mathbf{X}_1|^{(k+1)} + \sum_{j=1}^{i-1} \mathbf{dX}^1|^{(k)} \odot \mathbf{P}^{j-1}|^{(k)}\right) - \tilde{\mathbf{Y}}_i\right) \odot \left(\sum_{j=3}^i (j-2) \overline{\mathbf{dX}^1|^{(k)}} \odot \overline{\mathbf{P}^{j-3}|^{(k)}}\right)\right)$
 - 5: $\mathbf{P}|^{(k+1)}$ from (15)
 - 6: {Updating \mathbf{dX}^1 } $\mathbf{dX}^1|^{(k+0.5)} \leftarrow \mathbf{dX}^1|^{(k)} - \gamma_3 \times$
 $\sum_{i=2}^I \left(\Phi_B^0\left(\Phi_F^0\left(\mathbf{X}_1|^{(k+1)} + \sum_{j=1}^{i-1} \mathbf{dX}^1|^{(k)} \odot \mathbf{P}^{j-1}|^{(k+1)}\right) - \tilde{\mathbf{Y}}_i\right) \odot \left(\sum_{j=2}^i \overline{\mathbf{P}^{j-2}|^{(k+1)}}\right)\right)$
 - 7: $\mathbf{dX}^1|^{(k+1)}$ from (16)
 - 8: $k \leftarrow k + 1$
 - 9: **end while**
 - 10: {Output} $\mathbf{P} \leftarrow \mathbf{P}|^{(K)}$; $\mathbf{X}_d \leftarrow \mathcal{T}(\mathbf{dX}^1|^{(K)} \odot (\mathbf{P} - \mathbf{1}), \psi)$ on $\text{supp}(\mathbf{dX}^1|^{(K)})$; $\mathbf{X}_s \leftarrow \mathbf{X}_1|^{(K)} - \mathbf{X}_d$
-

accurately estimated when the target is mixed with significant clutter energy. These scenarios are common, especially in urban environments.

E. Moving Target Imaging and State Estimation

Given the estimated reflectivities of the decoupled moving targets \mathbf{X}_d , in this processing stage we extend the analysis to the full states of selected targets and enhance the moving target imaging. The detailed processing pipeline of this stage is depicted in Fig. 4.

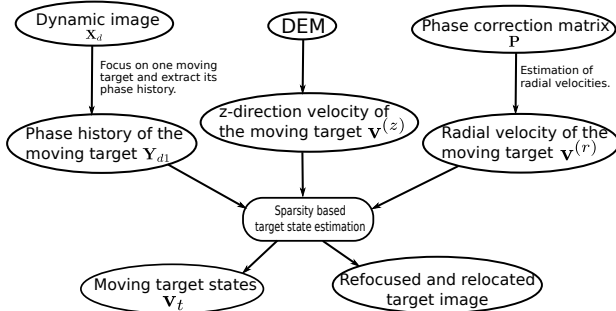


Fig. 4: The moving target imaging and target state estimation stage of the proposed framework.

Let us focus on one moving target of interest and extract its reflectivities \mathbf{X}_{d1} from \mathbf{X}_d using a rectangular window. We first derive the velocity coded backward projection operator for moving targets by incorporating the target velocity vector in the estimation of differential ranges (10). Let the target velocity vector be $\mathbf{v}_t = (v^{(x)}, v^{(y)}, v^{(z)})$ and the subdata $\mathbf{Y}_{d1} = \Phi_F^0(\mathbf{X}_{d1})$. The image formation of this moving target

with the DEM and known velocities can be organized as:

$$\mathbf{X}_{d1}(m, l) = \sum_{k=1}^K \sum_{n=1}^N \mathbf{Y}_{d1}(f_k, \tau_n) \times \exp\left(\frac{j4\pi f_k (\|\mathbf{r}(\tau_n) - \mathbb{G}_{ml} - \mathbf{v}_t \tau_n\| - \mathbf{R}_0(\tau_n))}{c}\right) \quad (19)$$

where the enhanced differential ranges $\Delta \mathbf{R}'_{mln} = \|\mathbf{r}(\tau_n) - \mathbb{G}_{ml} - \mathbf{v}_t \tau_n\| - \mathbf{R}_0(\tau_n)$ are used to replace the $\Delta \mathbf{R}_{mln}$ in (10). If we only have the estimated radial velocity, the differential ranges can be approximated with:

$$\begin{aligned} \Delta \mathbf{R}'_{mln} &\cong \|\mathbf{r}(\tau_n) - \mathbb{G}_{ml}\| + v^{(r)} \tau_n - \mathbf{R}_0(\tau_n) \\ &= \|\mathbf{r}(\tau_n) - \mathbb{G}_{ml}\| - \mathbf{R}'_0(\tau_n) \end{aligned} \quad (20)$$

where $\mathbf{R}'_0(\tau_n) = \mathbf{R}_0(\tau_n) - v^{(r)} \tau_n$, and $v^{(r)}$ stands for the radial velocity with which the target moves away from the platform.

In this work the moving target imaging and relocation are realised with (19) and (20). It can be seen that the full target states can be naturally embedded in the fast SAR imaging mechanism [14] by fixing the differential ranges with pre-calculated constant vectors. Based on (19), we denote the enhanced imaging operator using target velocities and the DEM as Φ_B^V and its Hermitian transpose as Φ_F^V .

Having defined the moving target imaging operators, we now give an insight into the role of sparsity in estimating the target states \mathbf{v}_t . This estimation requires us to consider the problem in a higher dimensional parameter space instead of the conventional physical coordinates space (x-y-z space). Let the velocity map of the whole observed scene be $\mathbf{V} = (\mathbf{V}^{(x)}, \mathbf{V}^{(y)}, \mathbf{V}^{(z)})$, in which $\mathbf{V}^{(x)} = \{v_{ml}^{(x)}\} \in \mathbb{R}^{M \times L}$, $\mathbf{V}^{(y)} = \{v_{ml}^{(y)}\} \in \mathbb{R}^{M \times L}$ and $\mathbf{V}^{(z)} = \{v_{ml}^{(z)}\} \in \mathbb{R}^{M \times L}$ represent the velocities of the image pixels in three directions. By combining \mathbf{V} with the physical space, we can set up an extended SAR processing space, and estimate the target

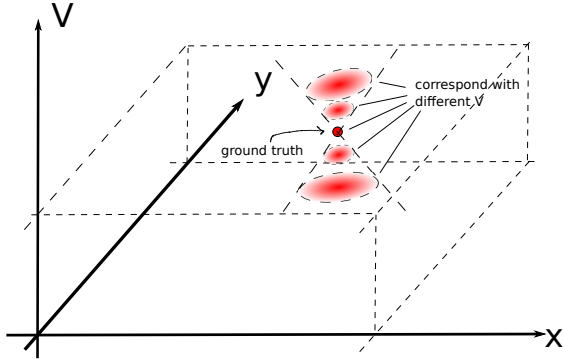


Fig. 5: The high dimensional space for the moving target imaging and estimation. The target states correspond with the sparsified image of this target.

states (positions, velocities, etc.) that correspond to the sparsest configuration in the space. As illustrated in Fig. 5, the moving target imaging task is equivalent to a search problem in a higher dimensional space, and the target can be better focused when the correct motion parameters are applied. Therefore, in this stage, the velocity estimation problem can be tackled by utilising the efficient projection operators and target sparsities:

$$\begin{aligned} \mathbf{v}_t &= \underset{\mathbf{v}^\dagger}{\operatorname{argmin}} \|\Theta^{\mathbf{v}^\dagger}(\mathbf{Y}_{d1})\|_1 \\ \text{s.t. } \mathbf{v}^\dagger &= \Upsilon(\mathbf{v}^{(z)}, \mathbf{v}^{(r)}) \\ \operatorname{supp}(\Theta^{\mathbf{v}^\dagger}(\mathbf{Y}_{d1})) &= \kappa \end{aligned} \quad (21)$$

where $\Theta^{\mathbf{v}^\dagger}$ is the approximated velocity compensated backward operator for the moving target, $\Theta^{\mathbf{v}^\dagger}(\mathbf{Y}_{d1})$ denotes the refocused and relocated image of the target after velocity and DEM compensation, κ is the support set (a 10-by-10 window in this paper) of the relocated target centered at the strongest pixel, and the target velocity obeys the geometrical constraint, $\mathbf{v}^\dagger = \Upsilon(\mathbf{v}^{(z)}, \mathbf{v}^{(r)})$, which represents the spatial constraint defined by the DEM and platform positions. Here we employ the L1 norm as the sparsity measure because L1 is a more tractable convex function compared to the L0 norm with guaranteed performance in sparse approximation problems [18]. $\mathbf{v}^{(r)}$ can be estimated directly from \mathbf{P} , and $\mathbf{v}^{(z)}$ can be estimated by differentiating the DEM based on target positions between neighbouring sub-apertures. Given the estimated $\mathbf{v}^{(r)}$ and $\mathbf{v}^{(z)}$, we can have $\mathbf{v}^{(x)}$ as a function of $\mathbf{v}^{(y)}$ and this optimisation problem becomes a simple one dimensional line search problem. To find the reflectivities that best fit the observed data in the least squares sense, we calculate $\Theta^{\mathbf{v}^\dagger}$ with the LSQR algorithm [19], as direct imaging operators such as (19) only approximately estimate the formed images and sacrifice the fidelity. In particular, the LSQR approximates the pseudo-inverse of the velocity compensated forward operator by implementing (19) in an iterative manner to better preserve the data consistency between the data \mathbf{Y}_{d1} and the formed image. For the rest of the paper, the data consistency stands for the data fitting fidelity that describes the goodness of fit between the data and formed SAR images. We form the moving target image $\Theta^{\mathbf{v}^\dagger}(\mathbf{Y}_{d1})$ for each target velocity vector \mathbf{v}^\dagger , and then select the \mathbf{v}^\dagger that gives the best

focused target image. Note that the DEM may have limited accuracy, but the estimated $\mathbf{v}^{(z)}$ can still be used as an auxiliary parameter in (21).

TABLE I: The system parameters of the AFRL GOTCHA GMTI challenge dataset.

platform start point (m)	(6675.4, 2938.8, 7259.4)
platform end point (m)	(5716.6, -4435.1, 7240.6)
first pulse number	907249
last pulse number	1061428
observation duration (s)	71
channel number	3
PRF (Hz)	2171.6
central frequency (Hz)	9.6G
bandwidth (Hz)	640M
phase history size	(5400, 154180)
range gating	384
moving target GPS start point (m)	(7.08, -154.9, 7.8)
moving target GPS end point (m)	(-363.7, 201.5, -10.2)

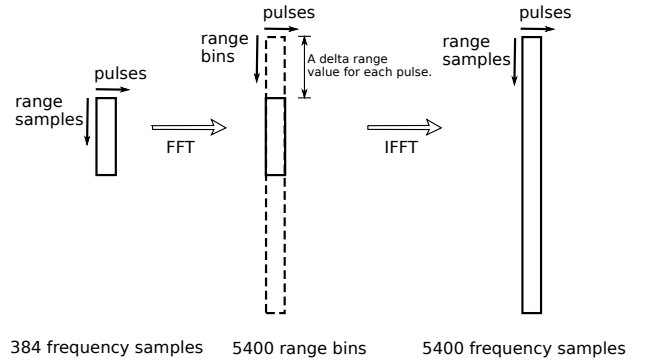


Fig. 6: The 384 frequency samples for each pulse are first transformed into 5400 range bins based on a delta range value in the original data (zeroes for unknown bins), and then transformed back into the 5400 range frequency samples.

IV. REAL DATA PERFORMANCE ANALYSIS

A. Dataset Description

In this section we demonstrate the proposed method through the AFRL GOTCHA data set [11]. The described data set comes from an X-band SAR system with three channels and a number of moving vehicles in a non-homogeneous urban environment. The ground truth data of one vehicle is provided. Its path is along a mountainous road which has significant elevation variations. In particular, the transmitted chirp is centred at 9.6 GHz, the phase history is collected over a 71 second interval, and the PRF f_{PRF} is 2.1716 kHz. The key system parameters are listed in Table I. Note that the original data was range-gated to decrease the required storage space. A frequency offset was used for each pulse to trim the frequency samples down to get 5400 frequency samples. To further decrease the storage and get the moving target centered within the range samples, a delta range value for each pulse

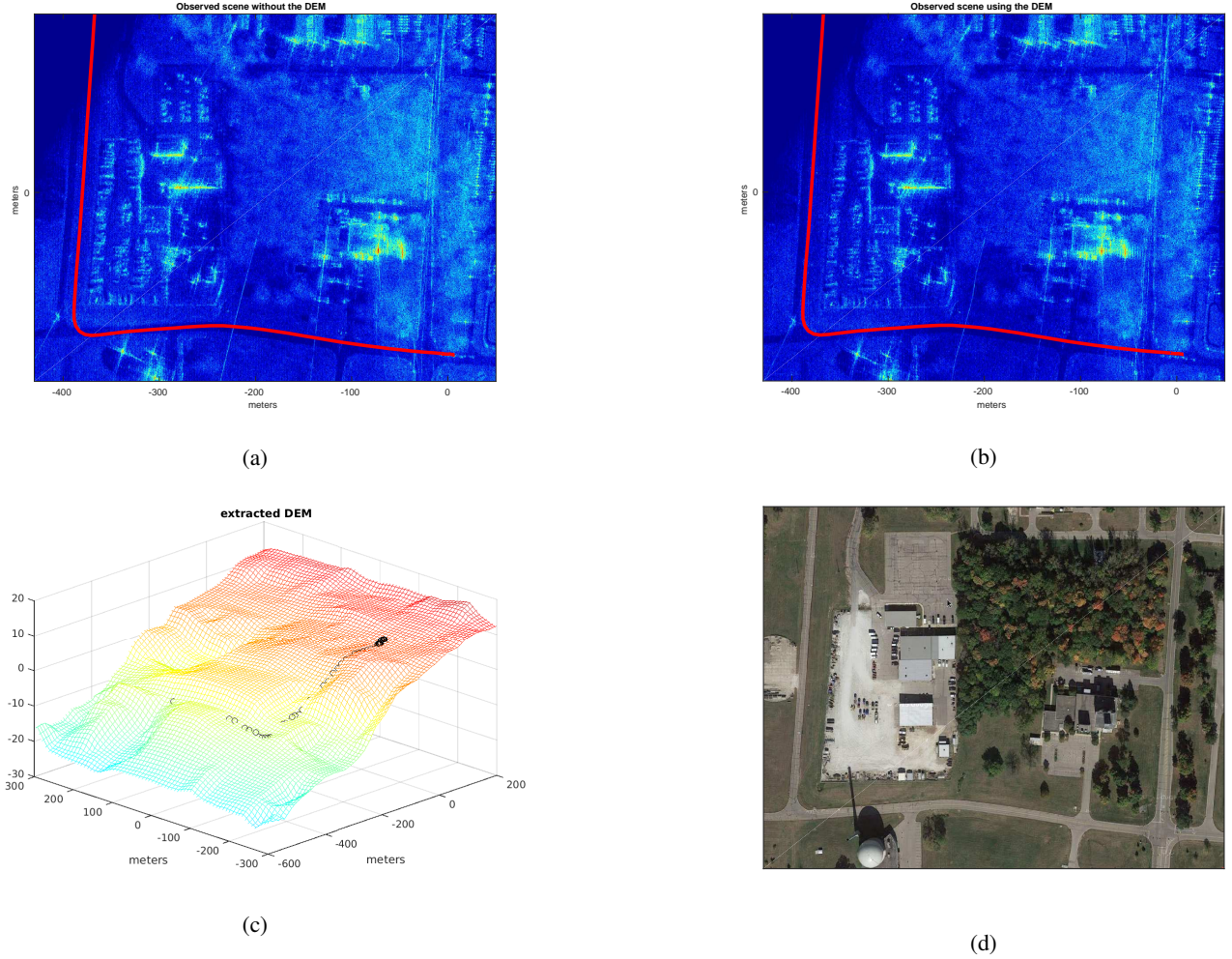


Fig. 7: a) and b) The reconstructed SAR image in dB using the range-gated data to show the GMTI scene without and with the DEM respectively. The red path stands for the target trajectory based on the ground truth data. c) The extracted terrain map. The black circles show the target trajectory. d) The corresponding Google map of this scene. Here we show a roughly extracted map and the coordinates may have small inconsistencies with our formed SAR images.

was estimated based on the target GPS to range-gate the data into 384 range bins. The detailed information of the range gating is presented in [11]. In this work we employ 5400 frequency samples for each pulse to implement the proposed SAR/GMTI framework, and the process for extracting this data is the inverse operation of the range gating which can be visualised in Fig. 6.

Unfortunately the AFRL data set does not have all information required. Firstly, no DEM information is provided in the dataset. To tackle this issue, we retrieved the coarse DEM data from the United States Geological Survey (USGS) seamless data set [20] (roughly 30 meters resolution). We adopted the method described in [21] to estimate a calibrated elevation map, and then interpolated the map on our imaging x-y grid (x_m, y_l) to get z_{ml} . We apply the DEM $\mathbb{G}_{ml} = (x_m, y_l, z_{ml})$ to all SAR processing in the rest of the paper.

Secondly, the antenna spacings between channels are unknown in the original data set. Here we estimate the spacings from the raw data. As shown in (7), the phases of the estimated

correction function $H_{az}(\omega)$ are approximately linear with ω , and this linear slope S_{az} is proportional to the channel spacing d . Consider the discrete signals with normalised frequencies, we can estimate the distance between two channels via:

$$d = \frac{S_{az} N_D v_p}{2\pi f_{PRF}} \quad (22)$$

where N_D denotes the number of azimuth samples. We implemented pair-wise estimations with (22) on the GOTCHA data set and got consistent results that the three antennas are equally spaced by $d = 0.238m$. This result coincides with the spacing estimates in [22].

Thirdly, the given ground truth information for the moving vehicle only covers its velocities in the x and y directions. Especially with this data set the monitored region has a non-flat terrain which results in nontrivial velocity components in the z direction. Based on the positions of the target in the ground truth, we differentiate its corresponding coordinates to estimate its velocities in the z direction $v^{(z)}$. We take the given

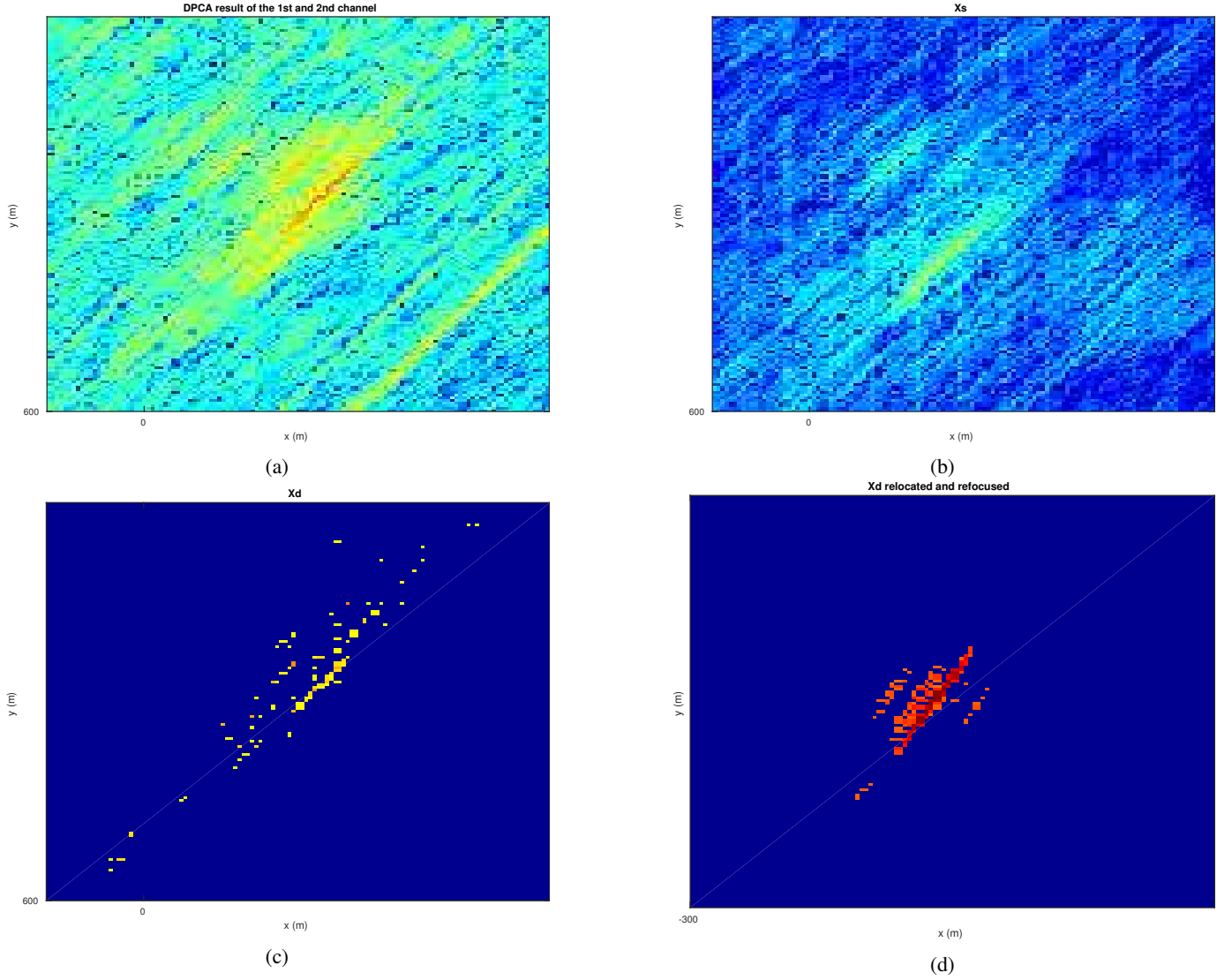


Fig. 8: a) The DPCA image between the 1-st and 2-nd channel centered at the target. b) The background image centered at the target. c) The SAR image of the moving target. d) The SAR image of the moving target after refocusing and relocation.

ground truth $v^{(x)}$, $v^{(y)}$ and the estimated $v^{(z)}$ as the baseline in this paper.

The monitored scene is shown in Fig. 7 which is synthesized using range-gated images generated with (10). Here the image quality can be degraded due to the missing data. The estimated DEM employed during the imaging process is shown in Fig. 7.b. Based on the ground truth data, the scene is overlaid with the target trajectory illustrated by the red path. It can be seen that there can be a displacement of 10 to 20 meters between the road and the target path along the x direction if we do not apply the DEM. Also it is shown in Fig. 7.c that the observed region has significant elevation variations. The corresponding Google map is shown in Fig. 7.d.

To preprocess the data, we implement the inverse operation of the range gating and replace the unknown range gates with zeroes. The phase history after this process is denoted as $\mathbf{Y}_i \in \mathbb{C}^{5400 \times 200}$ for the i -th channel. We then apply the aforementioned 2D channel balancing technique [13] pair-wise and denote the calibrated phase histories as $\tilde{\mathbf{Y}}_i$.

B. Moving Targets and Background Separation

In this section, the proposed decomposition framework as described in Algorithm 1 is implemented to decouple the moving targets and background. Then we directly estimate the radial velocities from \mathbf{P} for all image pixels within the nine sub-apertures. As we have estimated the velocity map for the whole image, the estimated velocities can vary from pixel to pixel and the accuracies of relocations are very sensitive to the estimated radial velocities. In this section we focus on the moving target for which we have the ground truth with a 15-by-15 window centered on the target in \mathbf{X}_d , and extract its phase history with $\mathbf{Y}_{d1} = \Phi_F^0(\mathbf{X}_{d1})$ as presented in section 3.E. To have a single velocity estimation $v^{(r)}$ for this target, we need to integrate these pixel-wise velocities. By assuming that the pixels with large magnitudes in \mathbf{X}_{d1} are likely to be our targets, we employ the weighted average within the window to estimate a single radial velocity, using weights proportional to the pixel magnitudes. The pixels which have

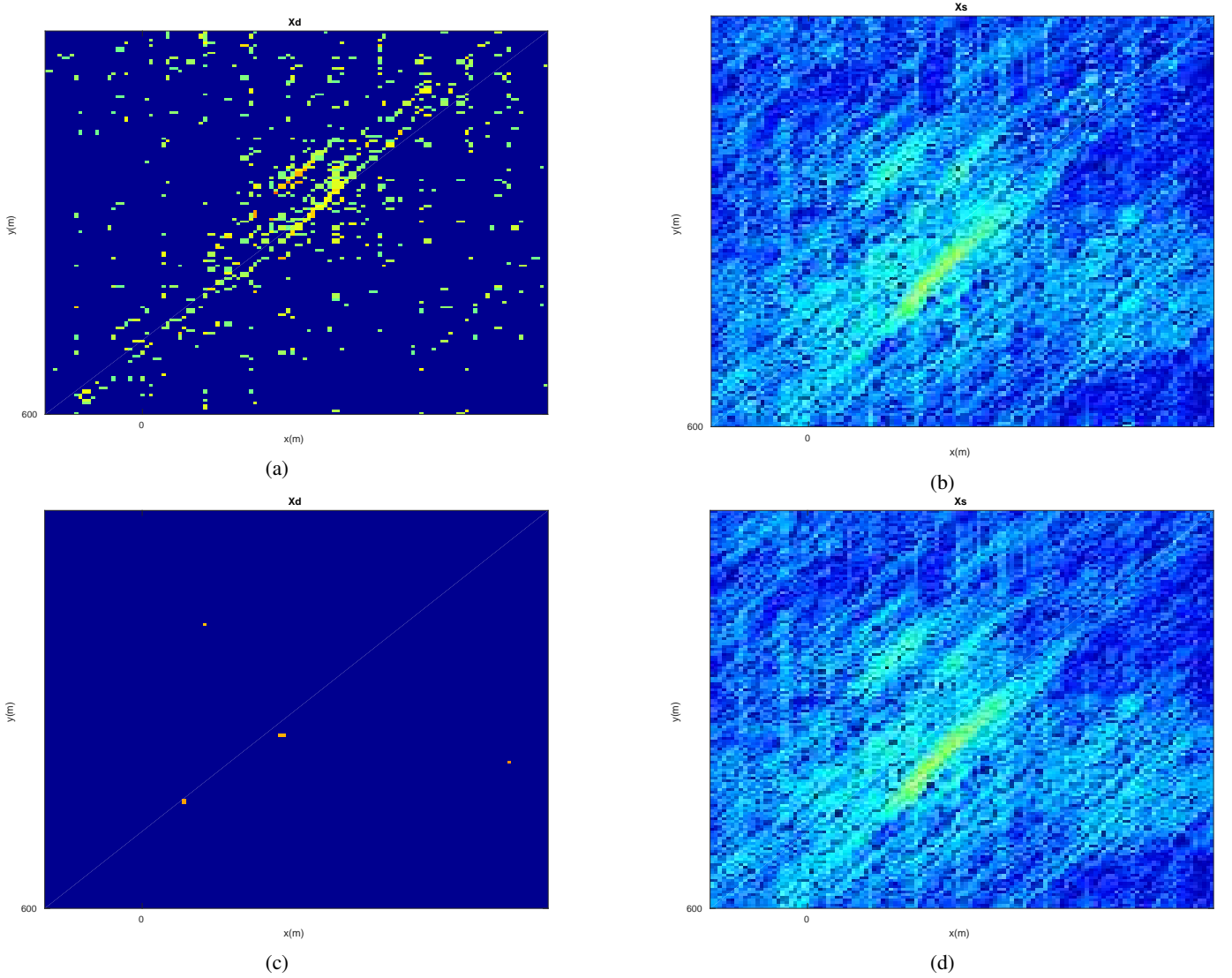


Fig. 9: a) and b) The SAR image of the moving target and background respectively. ($\psi = 0.12\% \|\mathbf{X}_d\|_F$ and $\varphi = 0.17$) c) and d) The SAR image of the moving target and background respectively ($\psi = 0.55\% \|\mathbf{X}_d\|_F$ and $\varphi = 1.5$)

significant deviations (larger than 2 m/s) from the estimated velocities are removed. With the estimated $v^{(r)}$, we apply the moving target imaging approach (19) to \mathbf{Y}_{d1} to localise the relocated target. A hybrid DPCA/ATI method (using pairwise DPCA and passing the results to ATI) is used as the baseline which was shown to outperform the pure ATI and DPCA [23] individually. (Note that, for a fair comparison, we employed the fast imaging operators [14] instead of the Doppler processing described in [23].)

A typical decomposition at the 50–th second is shown in Fig. 8. It can be seen that the proposed method decoupled the main energy of the target and the background (here we employ a typical $\psi = 0.35\% \|\mathbf{X}_d\|_F$ in Algorithm 1 by considering the aforementioned constraints on ψ). We consistently set $\varphi = 0.5$ in Algorithm 1, regardless of the sparsity of the scenarios among different snapshots, and this threshold controls how we retrieve the support of \mathbf{X}_d which leads to the balance of the energy allocation between \mathbf{X}_s and \mathbf{X}_d . Note that the essence of the proposed model is exploiting the priori information

(sparsity in \mathbf{X}_d) while preserving the data consistency. With this perspective, s compromises the balance between the data fidelity and signal sparsity. While a small s in (12) corresponds to a large ψ and φ in Algorithm 1, we can further demonstrate the crucial role of s in this decomposition via different settings. The results with different ψ and φ are visualised in Fig. 9. It can be seen from Fig. 9 a) that with a too large s the support of \mathbf{X}_d is very large and the false alarm rate is significantly high. With a too small s for Fig. 9 c), the objective function in (12) approximately matches \mathbf{Y}_i in different channels to a single \mathbf{X}_s which significantly corrupts the data consistency. The support of \mathbf{X}_d is thus too small and we miss the detection of targets.

In Fig. 10 we show how the cost function varies with iterations in the processing of this snapshot, demonstrating the non-increasing property. It is worth mentioning that the Algorithm 1 always works without triggering the backtracking mechanism in our experiments.

We processed nine sub-apertures centered at the 25–th, 30–th, 35–th, 40–th, 45–th, 50–th, 55–th, 60–th and

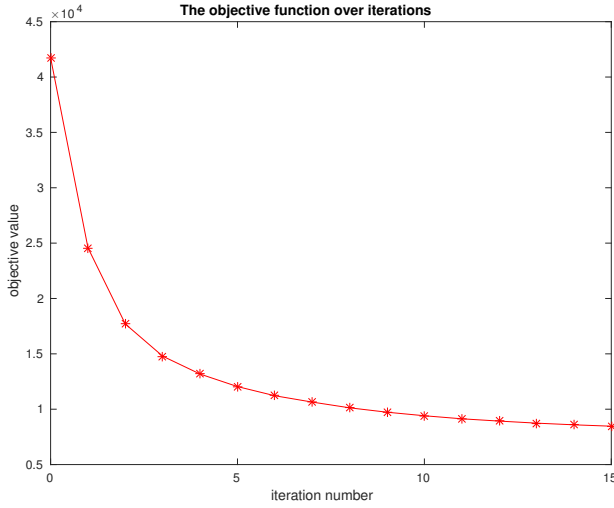


Fig. 10: The objective function of (14) with iterations.

65—th second respectively, and compared the estimated radial velocities to the ground truth in Fig. 11. Here we employed 3 and 15 iterations in Algorithm 1 respectively to compare the performance. We show the relocated target locations in Fig. 12. Each sub-aperture contains 400 azimuth samples (roughly 0.18 seconds). In Fig. 11 and Fig. 12 the proposed method is more accurate in estimating radial velocities and localising moving targets compared to the hybrid DPCA/ATI. With 15 iterations we received a better relocation and a smaller error on the radial velocity estimation. The proposed decomposition method gives better performance on the target/clutter decomposition with more iterations. Note that at the 55—th second, the scenario is challenging for conventional SAR-based GMTI techniques. Firstly, this sub-aperture corresponds to the moment that the target is mixed with a strong static clutter (buildings). It significantly hampered the correct estimation. Secondly, at this moment the vehicle is moving away from the antenna with 6.84 m/s. Note that the pixel-wise radial velocities are estimated based on the phase of \mathbf{P} . The phase wrapping leads to an estimation cycle on the radial velocities (the cycle is 6.6 m/s for this sub-aperture). The ground truth is very close to the cycle value which means that it is easily confused with zero velocities and the thresholding operations in (15) is likely to threshold certain components of the target which increases the estimation errors.

While the sparsity driven method in [9] is also capable of estimating the radial velocities, it is worth mentioning that the proposed method has differences in assumptions, sparse modalities and data consistency. The method in [9] assumes that there exist multiple velocity components at each SAR pixel (both moving ones and static ones), and it is possible to have a number of moving targets in each SAR pixel. The proposed method assumes the extracted dynamic image has no more than one moving target for each pixel. While [9] is exploiting the sparsities in pixel-wise radial velocity components, the proposed method is investigating the sparsities in the SAR reflectivities. The method in [9] sets up the pixel-wise sparse reconstruction model after a previous image formation

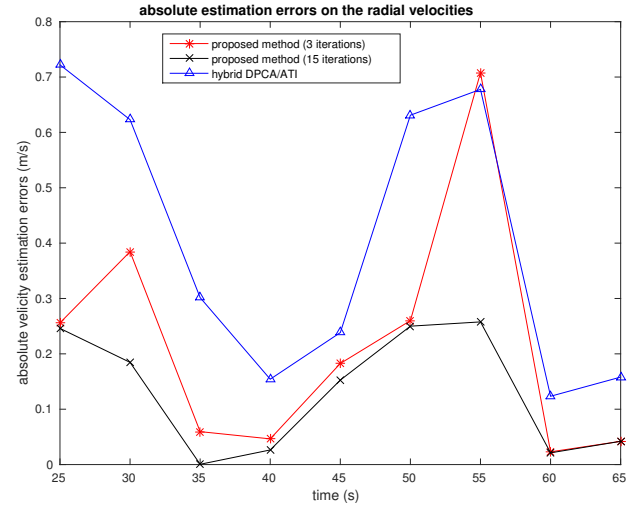


Fig. 11: The comparisons of the absolute estimation error (based on the ground truth) on the target radial velocity with the proposed approach and hybrid DPCA/ATI.

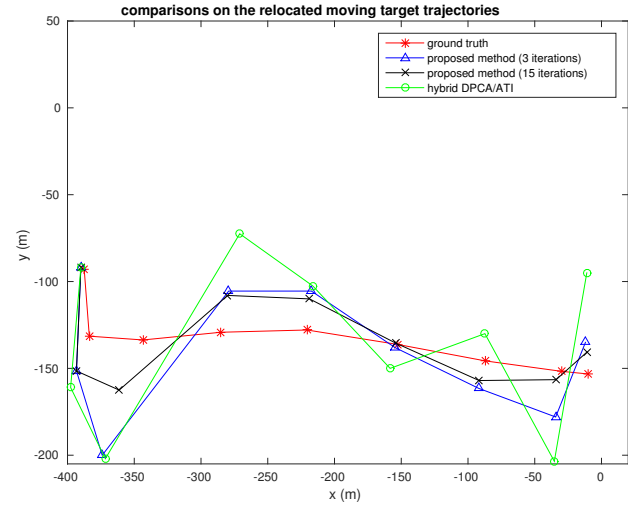


Fig. 12: The comparisons of the target relocations with the proposed approach and hybrid DPCA/ATI.

stage which can be taken as the post-processing the SAR imaging (similar to the DPCA and ATI algorithms). However, direct imaging operators sacrifice the data consistency in the approximation of the pseudo-inverse of the SAR forward operator. The proposed SAR/GMTI framework is designed to maximise the data consistency while employing the target sparsities through the iterative procedures. The improvement in the data consistency with the proposed framework brings significant estimation accuracy gain over other SAR/GMTI methods. We have implemented the method in [9] on the 50—th second for comparison. Specifically we normalised the projection matrix and measurement vector in [9] column-wise and employed the BPDN SPGL1 [24][25] with the sparsity variable $\sigma = 1$. The estimated radial velocity map for this snapshot can be found in Fig. 13. The estimated radial velocity of the target at 50—th second is -0.71 m/s (Fig. 13). By shifting this estimated velocity with the estimation cycle

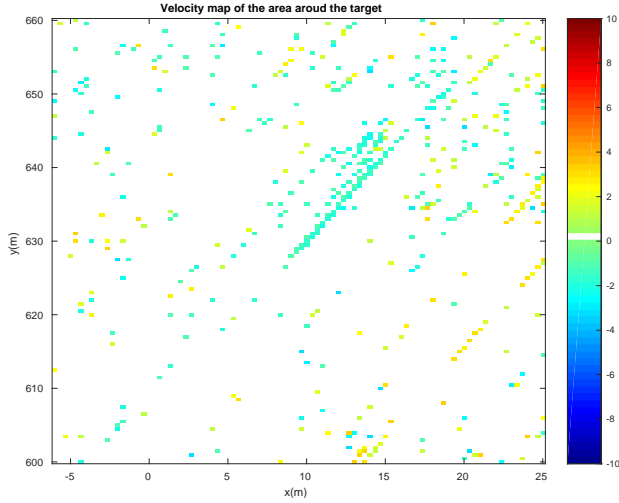


Fig. 13: The estimated radial velocity map at the 50–th second. Here we only mark the pixels with velocity above 1 m/s for proper visualisation. This velocity map can be further marked by thresholding on image magnitudes to detect the moving targets.

(due to the phase wrapping), the estimated radial velocity is -7.48 m/s. The ground truth radial velocity is -8.16 m/s, and the estimated radial velocities of other methods are -7.91 m/s (proposed method with 15 iterations) and -7.5 m/s (hybrid DPCA/ATI). It can be seen that the estimation accuracy of [9] is very close to that of the hybrid DPCA/ATI.

C. Velocity Estimation and Target Imaging

We have estimated the radial velocity of the target, and extracted the phase history of this target \mathbf{Y}_{d1} (we choose the 15-iteration results from the previous processing stage). In this section, we estimate its full velocity vector \mathbf{v}_t and further image the target based on the estimated \mathbf{v}_t . The model (21) is first introduced to estimate the \mathbf{v}_t . In particular, for far-field observation, the target velocity components obey the geometrical restriction Υ which can be transformed into:

$$v^{(r)} \approx -\langle v^{(x)}, \frac{\mathbf{r}_1^{(o)}}{r_1^{(o)}} \rangle - \langle v^{(y)}, \frac{\mathbf{r}_1^{(o)}}{r_1^{(o)}} \rangle - \langle v^{(z)}, \frac{\mathbf{r}_1^{(o)}}{r_1^{(o)}} \rangle \quad (23)$$

where negative $v^{(r)}$ means that the target is moving away from the platform. As $v^{(z)}$ is in general not too large in most scenarios, we can approximate it by differentiating the coordinates of the relocated target at different frames. Given the estimated $v^{(r)}$ and (23), $v^{(x)}$ is a function of $v^{(y)}$. In (21), we simply traverse $v^{(y)}$ from 0 m/s to line search for our estimations. The target image $\Theta^{v_t}(\mathbf{Y}_{d1})$ for each velocity vector \mathbf{v}_t is formed via two iterations of LSQR to obtain good data fidelity. By searching for the minimised $\|\Theta^{v_t}(\mathbf{Y}_{d1})\|_1$, we find the estimated \mathbf{v}_t that gives the sparsest image. We compare the estimated target velocities to the ground truth in x, y and z directions respectively, and show the absolute estimation errors in Fig. 14. Furthermore, the target state estimation methods in state-of-the-art algorithms EDPCA [7] and ISTAP [5] maximise the generalised likelihood ratio tests

(GLRT) for image pixels. They essentially search for the motion parameters to best focus the moving targets in the image domain. We adopt this idea to maximise the GLRT on the relocated target spot and search for the target state that gives the maximised energy. The results are presented in Fig. 14 for comparison. The absolute estimation errors for the velocity components with different methods are visualised via error bars. We also show the relocated and refocused target image of the 50–th second in Fig. 8.d.

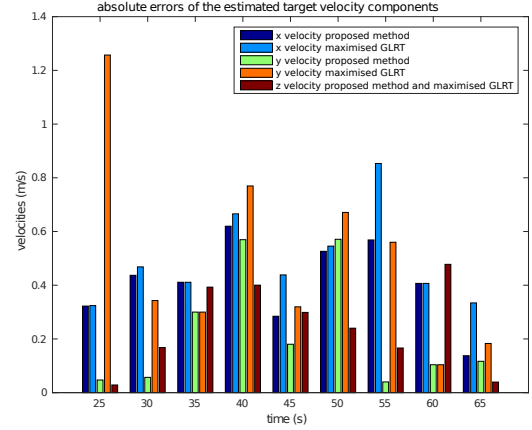


Fig. 14: The comparisons on the absolute estimation errors of target velocity components.

As the velocity components of the moving target in the z direction are usually not too large in reality, they are roughly estimated by differentiating the physical coordinates. We employ the same $v^{(z)}$ estimation for the proposed method and the maximised GLRT method. Although direct differentiation has limited accuracy, it can be seen from Fig. 14 that the estimation on $v^{(z)}$ matches the ground truth in most scenarios. In addition, it is shown in Fig. 14 that the proposed sparsity-aided approach achieves better estimation accuracies on $v^{(x)}$ and $v^{(y)}$ than the maximised GLRT method (lower error bars). The accuracy improvement is likely to come from the assumption of the target pattern and data consistency (the fitting fidelity between the data and the reconstructed image). Particularly the maximised GLRT method considers the estimation problem pixel-wise and it maximises the response with different velocity configurations for each pixel. In this work we assume that the target consists of multiple pixels, and we aim to find the parameters to best focus the moving targets for each target pattern. The data consistency is likely to be improved by matching a target to multiple pixels instead of a single pixel. The proposed state estimation has further potential to be combined with the previous processing stage as they are both exploiting the target sparsities.

V. CONCLUSION

This paper presents a complete SAR/GMTI framework for separating moving targets from the background, estimating the states of the targets, and relocating and refocusing the targets under multi-channel SAR scenarios. The framework is motivated by integrating SAR/GMTI tasks into a sparsity

regularised optimisation problem. The proposed methods are able to implement decompositions of moving targets and the background instead of simple target detection. The DEM information can be leveraged to enhance the process. A two stage process is designed to tackle the framework in practice considering the difficulties in computational load and forward/backward operators. Specifically, after the pre-processing, at the first stage we build up a sparsity based model with an iterative decomposition algorithm. The SAR images of the background and moving targets can be formed, and the radial velocities of the moving targets can be estimated. In the next stage, we estimate the full states of the targets by searching the feasible velocity space to best sparsify the moving target image. Given the estimated states of moving targets, they can be better imaged and localised.

The performance of the proposed methods is demonstrated through the AFRL GOTCHA GMTI challenge. By comparing to the ground truth data, a hybrid ATI/DPCA approach, and a maximised GLRT method, we show the results in terms of target localisation and state estimation. While the proposed methods provide accurate decomposition and state estimation, they are computationally intensive even though fast operators have been used. Efficiently approximating our proposed framework, simplifying the processing pipeline, and pursuing better GMTI accuracy, especially with strong clutter, are the open challenges to be investigated in the future.

ACKNOWLEDGMENT

This work was supported by the Engineering and Physical Sciences Research Council (EPSRC) grant [EP/K014277/1], part of the University Defence Research Collaboration (UDRC) in Signal Processing.

REFERENCES

- [1] R. Deming, M. Best, and S. Farrell, "Simultaneous SAR and GMTI using ATI/DPCA," *Proc. SPIE*, vol. 9093, pp. 90930U–90930U–19, 2014.
- [2] S. Chiu and C. Livingstone, "A comparison of displaced phase centre antenna and along-track interferometry techniques for RADARSAT-2 ground moving target indication," *Canadian Journal of Remote Sensing*, vol. 31, no. 1, pp. 37–51, 2005.
- [3] I. Sikaneta and C. Gierull, "Ground moving target detection for along-track interferometric SAR data," in *Aerospace Conference, 2004. Proceedings. 2004 IEEE*, vol. 4, March 2004, pp. 2227–2235 Vol.4.
- [4] J. Ward, "Space-time adaptive processing for airborne radar," in *Space-Time Adaptive Processing (Ref. No. 1998/241), IEE Colloquium on*, Apr 1998, pp. 2/1–2/6.
- [5] D. Cerutti-Maori, I. Sikaneta, and C. H. Gierull, "Optimum SAR/GMTI processing and its application to the radar satellite RADARSAT-2 for traffic monitoring," *IEEE Transactions on Geoscience and Remote Sensing*, vol. 50, no. 10, pp. 3868–3881, Oct 2012.
- [6] B. Liu, K. Yin, Y. Li, F. Shen, and Z. Bao, "An improvement in multichannel SAR-GMTI detection in heterogeneous environments," *IEEE Transactions on Geoscience and Remote Sensing*, vol. 53, no. 2, pp. 810–827, Feb 2015.
- [7] D. Cerutti-Maori and I. Sikaneta, "A generalization of DPCA processing for multichannel SAR/GMTI radars," *IEEE Transactions on Geoscience and Remote Sensing*, vol. 51, no. 1, pp. 560–572, Jan 2013.
- [8] D. Wu, M. Yaghoobi, and M. Davies, "A new approach to moving targets and background separation in multi-channel SAR," in *2016 IEEE Radar Conference*, 2016.
- [9] L. Prunte, "GMTI from multichannel SAR images using compressed sensing," in *Synthetic Aperture Radar, 2012. EUSAR. 9th European Conference on*, April 2012, pp. 199–202.
- [10] D. Wu, M. Yaghoobi, and M. Davies, "Sparsity based ground moving target imaging via multi-channel SAR," in *Sensor Signal Processing for Defence (SSPD), 2015*, Sept 2015, pp. 1–5.
- [11] S. M. Scarborough, C. H. Casteel, Jr., L. Gorham, M. J. Minardi, U. K. Majumder, M. G. Judge, E. Zelnio, M. Bryant, H. Nichols, and D. Page, "A challenge problem for SAR-based GMTI in urban environments," *Proc. SPIE*, vol. 7337, pp. 73 370G–73 370G–10, 2009.
- [12] J. H. G. Ender, P. Berens, A. R. Brenner, L. Rossing, and U. Skupin, "Multi-channel SAR/MTI system development at FGAN: from AER to PAMIR," in *IEEE International Geoscience and Remote Sensing Symposium*, vol. 3, June 2002, pp. 1697–1701 vol.3.
- [13] C. Gierull, "Digital channel balancing of along-track interferometric SAR data," in *Technical Memorandum DRDC Ottawa TM 2003-024*. Defence R&D, Ottawa, Canada, March 2003.
- [14] S. Kelly and M. Davies, "A fast decimation-in-image back-projection algorithm for SAR," in *Radar Conference, 2014 IEEE*, May 2014, pp. 1046–1051.
- [15] T. Blumensath and M. E. Davies, "Iterative hard thresholding for compressed sensing," *Applied and Computational Harmonic Analysis*, vol. 27, no. 3, pp. 265 – 274, 2009.
- [16] T. Blumensath and M. E. Davies, "Iterative Thresholding for Sparse Approximations," *Journal of Fourier Analysis and Applications*, vol. 14, no. 5–6, pp. 629–654, Dec. 2008.
- [17] A. Beck and M. Teboulle, "A Fast Iterative Shrinkage-Thresholding Algorithm for Linear Inverse Problems," *SIAM Journal on Imaging Sciences*, vol. 2, no. 1, pp. 183–202, Mar. 2009.
- [18] E. J. Candes, "The restricted isometry property and its implications for compressed sensing," *Comptes Rendus Mathematique*, vol. 346, no. 9, pp. 589 – 592, 2008.
- [19] C. C. Paige and M. A. Saunders, "LSQR: An algorithm for sparse linear equations and sparse least squares," *ACM Trans. Math. Softw.*, vol. 8, no. 1, pp. 43–71, Mar. 1982.
- [20] ZONUMS, "USGS seamless elevation data sets," *NASA EOSDIS Land Processes DAAC, USGS Earth Resources Observation and Science (EROS) Center, Sioux Falls, South Dakota*, 2010.
- [21] D. Wu, M. Yaghoobi, and M. Davies, "Digital elevation model aided SAR-based GMTI processing in urban environments," in *Sensor Signal Processing for Defence (SSPD), 2016*, Sept 2016, pp. 1–5.
- [22] B. Guo, D. Vu, L. Xu, M. Xue, and J. Li, "Ground moving target indication via multichannel airborne SAR," *IEEE T. Geoscience and Remote Sensing*, vol. 49, no. 10, pp. 3753–3764, 2011.
- [23] R. W. Deming, S. MacIntosh, and M. Best, "Three-channel processing for improved geo-location performance in SAR-based GMTI interferometry," *Proc. SPIE*, vol. 8394, pp. 83 940F–83 940F–17, 2012.
- [24] E. van den Berg and M. P. Friedlander, "Probing the pareto frontier for basis pursuit solutions," *SIAM Journal on Scientific Computing*, vol. 31, no. 2, pp. 890–912, 2008. [Online]. Available: <http://link.aip.org/link/?SCE/31/890>
- [25] E. van den Berg and M. P. Friedlander, "SPGL1: A solver for large-scale sparse reconstruction," June 2007, <http://www.cs.ubc.ca/labs/scl/spgl1>.